Arab J Geosci (2013) 6:3493–3503
DOI 10.1007/s12517-012-0577-7

ORIGINAL PAPER

Imaging soil moisture using GPR tomography and reflection field experiments

Mohamed G. El-Behiry · Sherif M. Hanafy

Received: 18 December 2011 / Accepted: 3 April 2012 / Published online: 15 May 2012

Abstract We performed GPR tomography and GPR reflection field experiments using a 500-MHz antenna to image relative soil moisture distribution around a poplar tree at the botanic garden of Kiel University, Kiel, Germany. The GPR tomography field experiment is carried out in two consecutive phases in order to obtain ray paths traveling from all directions and intensively covering the target. The radar tomographic data are inverted using the authors' developed software code *SeismoRad* based on the finite difference technique. The attained Root-Mean-Square (RMS) errors after 200 iterations between the measured and calculated times range between 1.066 and 5.7 % in the two tomography experiments. The estimated GPR velocities range between 5.3 and 15.1 cm/ns. Two low-GPR velocity zones could be delineated coinciding with the locations of the tree root zone and a previously excavated sector. The high water saturation zone around the tree root system is found to be the main reason for such a decrease in GPR velocity. Interpretation of the two phases proved that the coverage of ray paths from all directions is important to delineate the effect of the poplar tree root system and hence to obtain accurate tomographic results. Furthermore, four GPR reflection lines are performed along the sides of the four trenches such that the antenna is moved longitudinally in the trenches and the radargrams are recorded along the horizontal *xy*-plane parallel to the ground surface. On the processed GPR reflection radargrams, relatively high-amplitude GPR anomalies could be outlined and are attributed to the boundary between the saturated and wet zones where different water contents affect the GPR velocity. Comparable results are obtained between the tomogram and the radar reflection results with respect to zones of increase in water content.

Keywords GPR · Tomography · Moisture content · Poplar tree

M. G. El-Behiry (✉) · S. M. Hanafy
Geophysics Department, Faculty of Science, Cairo University,
Giza, Egypt
e-mail: el_behiry@yahoo.com

M. G. El-Behiry
Geophysics Department, Faculty of Earth Sciences,
King Abdulaziz University,
Jeddah, Saudi Arabia

S. M. Hanafy
King Abdullah University for Science and Technology (KAUST),
Jeddah, Saudi Arabia

Introduction

Ground penetrating radar (GPR) is applied to a wide range of scientific fields as non-invasive tool for mapping sedimentary structures (Neal 2004), depth of reflecting surfaces such as ground water table (van Overmeeren et al. 1997; Roth et al. 2004; Annan 2005), or permafrost tables (Hinkle et al. 2001; Moorman et al. 2003), as well as for estimating volumetric soil-water content and soil moisture (Huisman et al. 2003; Wollschlaeger et al. 2004; Wollschlaeger and Roth 2005; Hanafy and Hagrey 2006; Gerald et al. 2008). For hydrogeophysical studies, GPR is applied increasingly in combination with hydrologic measurements to obtain hydraulic properties (Lambot et al. 2004; Kowalsky et al. 2005).

Existence of liquid component within the scanned sediments has a major role to play in electrical properties due to the high dielectric constant of water (80) compared to that of most earth forming minerals (approximately 4 to 12). Therefore a change in the water content can cause a dielectric change where no sedimentological change exists (Rea and Knight1998). Commonly, strong GPR reflections are

obtained due to increase in water content within the sediments (Huisman et al. 2003, Hanafy and Hagrey 2006).

The scope of the present study is to compare between the commonly known GPR reflection profiling and GPR tomography to image soil moisture. The principles of both modes of radar measurement are briefly discussed. Field radar experiments using both survey modes are described and the obtained results of each are explained and evaluated. The results of the present study will emphasize the ability of GPR tomography technique as rapid and cost-effective tool in agriculture investigations. This includes the ability to map the roots of trees, identify locations that are more vulnerable to pollution by fertilizers, and thus help in isolating and proper disposal of contaminated areas, soil mapping, and analysis of soil to locate water pockets, and investigating the variability of soil properties.

GPR tomography

Recent researches in GPR tomography technique shows that tomography data offer exciting potential for subsurface characterization efforts (Peterson 2001). GPR tomography is increasingly used to characterize the shallow subsurface such as detection of wet zones; cavities and voids; monitoring hydrologic infiltration and transportation through saturated zones; delineating fractured rocks; aquifer sedimentology studies, and in many other applications (Baumgardt et al. 1995; Valle and Zanzi 1996; Hubbard et al. 1997; Vasco et al. 1997; Asprion 1998; Cai and McMechan 1999; Peterson 2001; Schmalholz et al. 2004).

The strategy for tomographic inversion of GPR data is based on the same assumptions as those required for the valid use of GPR. Solving the tomography problem depends mathematically on iteratively solving a system of linear equations (Gerald and Wheatley 1989; Menke 1989). The principle of the tomographic method shows a typical ray path from a transmitter to a receiver R_i (Fig. 1). With multiple transmitter and receiver arrays there would be a number of such rays crossing the intervening material in different directions.

The region between transmitter and receiver lines are discretized into cells each of area (a) and the slowness s_j of the cell j is assumed to be constant over the area covered by any one cell. The recorded travel time (t_i) can be expressed as integral over the ray path (Eq. 1).

$$t_i = \int_{R_i} S(x,y)da \tag{1}$$

Each of these integrals, in discrete form, becomes one equation in the linear tomographic system that is to be inverted for velocity and/or layer shape from travel times or for attenuation from amplitudes (Cai and McMechan 1999). The linear system of equations has the following form:

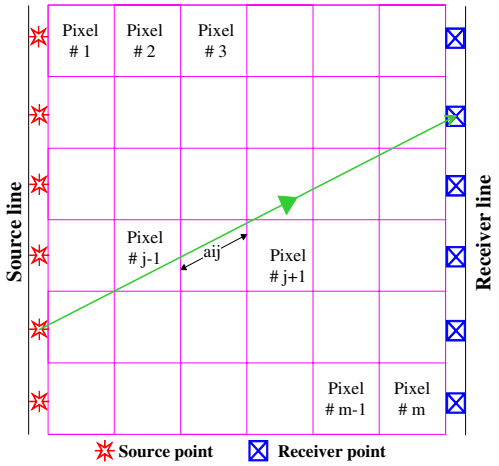

Fig. 1 Pixel geometry and ray path from source to receiver. For the ray i the distance traveled in a pixel j is denoted by a_{ij}

$$t_i = \sum_{j=1}^{m} \Delta\, a_{ij}\, S_j \quad \text{i=1,2,....,k} \tag{2}$$

where Δa_{ij} is the length of the ray i which penetrates pixel j, m is the total number of pixels intersected by the ray i, and s_j is the slowness of pixel j. In matrix notation, this is written as $t = As$ where t is the time vector, A is the distance matrix that connects the transmitter–receiver locations, and s is the slowness vector. This linear system of equations is solved using iterative technique to give the final velocity field of the area between a line of sources and a line of receivers.

Practically, the tomography inversion problem is solved by creating an initial slowness model s_o in each cell by simple matrix inversion of the data (e.g., Gaussian Elimination Method) or by specifying a reasonable model. The Finite Difference (FD) method (Vidale 1990 and modified by Hole and Zelt 1995) is employed to calculate travel time field for direct, refracted, or head waves in arbitrarily initial complex velocity models.

The FD method is also employed to solve for bending ray paths that connect sources and receivers rather than the approach of straight ray paths, which is not the case in real problems (Fig. 1). The main advantages for using the FD approach in solving tomographic problems are the accurate calculation of first arrival times, the exact tracing of ray path from receivers back to the source, and its capability to solve shadow zone and diffraction point problems. Two approaches are widely used to minimize the error between the observed and calculated travel time field via the FD method (Lo and Inderwiesen 1994); the Algebraic Reconstruction Technique and the Simultaneous Iterative Reconstruction Technique.

A specially developed PC-code namely *SeismoRad* (Hanafy 2002) is developed to analyze, display, and interpret GPR and seismic tomography data (Fig. 2). The input data are represented by the digitized recorded GPR travel times in nanoseconds and the transmitter–receiver offset in centimeters. The output is the calculated GPR velocity tomogram. *SeismoRad* will be employed in the present research to calculate radar tomograms resulted from field experiments and to interpret these tomograms in terms of soil moisture content.

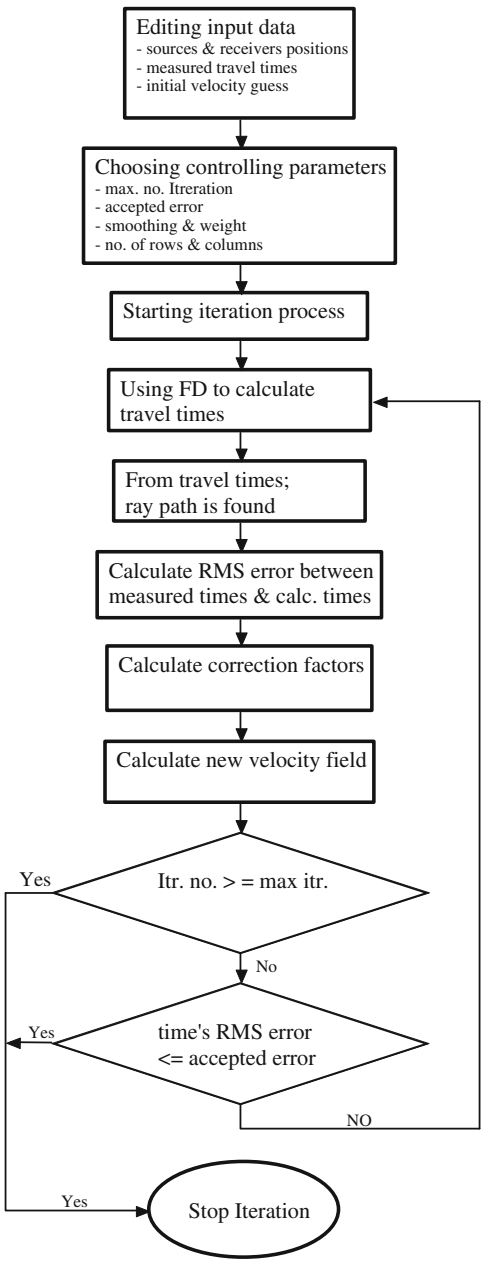

Fig. 2 Flowchart showing the iteration process for computing velocity tomograms using *SeismoRad* PC-code

Radar reflection profiling

In GPR profile measurement mode, the transmitting (Tx) and receiving (Rx) antennas are moved simultaneously over the ground, providing a continuous record of the varying elevations of the reflection surfaces and the locations of isolated bodies. Figure 3 shows the procedure involves repetitive moves of both Tx and Rx at a constant spacing. If the radio-wave velocities have been measured, then depths to reflectors can be determined. Identification of significant anomalies on a GPR records is a pattern recognition process of recognizing features on the records that are characteristic of known signatures. Identifiable features on reflection radar record fall into three main categories (Davis and Annan 1989):

1 Continuous reflection from horizontally layered geologic horizons,
2 Reflections from 2D and 3D objects, and
3 Lateral discontinuities that cause an abrupt change in the signal amplitude, diffractions, or a termination of adjacent reflections

Continuous, layered, one-dimensional, boundaries are usually the most difficult features to identify on a GPR record. Unless the boundaries are dipping, a reflection from a shallow horizontal boundary often interferes with other shallow reflections and ringing from the antenna. Reflections from small 2D and 3D buried objects (buried pipe and lines, barrels …etc.) can be identified by their small, characteristic hyperbolic shapes. Lateral discontinuities can cause either a change in the trend of the continuous reflections, and diffractions, or a change in the amplitude and phase of the signal. A lateral change in amplitude and phase is often associated with changes in the surface of the ground.

GPR field experiments

GPR tomography and reflection experiments are performed at the botanic garden of Kiel University, Kiel, Germany,

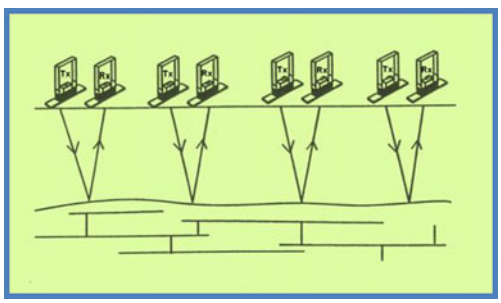

Fig. 3 GPR reflection survey mode

where the root of a poplar tree is selected to be the target (Hanafy 2002). The SIR10A instrument (Geophysical Survey Systems, Inc., GSSI) and a pair of moderately high-frequency antennae 500 MHz are used in acquiring radar field data of the present research.

GPR tomography experiment

The field GPR tomography experiment is carried out in two phases. In the first phase, two approximately parallel trenches (length=225 cm, width=40 cm, depth=50 cm each) are prepared at the botanic garden of Kiel University, Germany (Fig. 4a). Here, radar rays are expected to travel in only one direction. A total of 1,044 readings are recorded by utilizing 29 Tx and 36 Rx located in the two trenches with inter-receiver separation of 5 cm and inter-transmitter separation of 5 cm for Tx=1–22 and of 10 cm for Tx=23–29 (Fig. 4b). Figure (4c) shows four samples from processed radargrams used to provide radar time necessary for tomography inversion.

In the second phase, new acquisition is carried out at the same site to enhance the calculated tomogram and overcome the drawbacks of the first survey. The two existing trenches are extended to a length of 260 cm so that the poplar tree is in the middle of the surveying zone (Fig. 5a). Two new trenches of lengths 190 and 225 cm are excavated, to the same width and depth around the poplar tree and perpendicular to the old trenches. A number of 65 Tx and 57 Rx locations are set along the four sides of the trenches (Fig. 5b). A total of 2,213 GPR readings are recorded with Tx and Rx intervals of 10 cm. Hence, GPR tomography acquisition can be performed from all directions around the surveying zone. Figure 5c shows four samples of processed radargrams used to provide travel time data required for second-phase tomography inversion.

GPR reflection survey

Four conventional GPR reflection lines (a–b, b–c, c–d, and d–a) are performed along the sides of the four trenches, in the botanic garden (Fig. 5a). The width and depth of each trench are 40 and 50 cm, respectively. The monostatic 500-MHz antenna is held vertically against the inner wall of the trench and moved along to map a horizontal slice of the

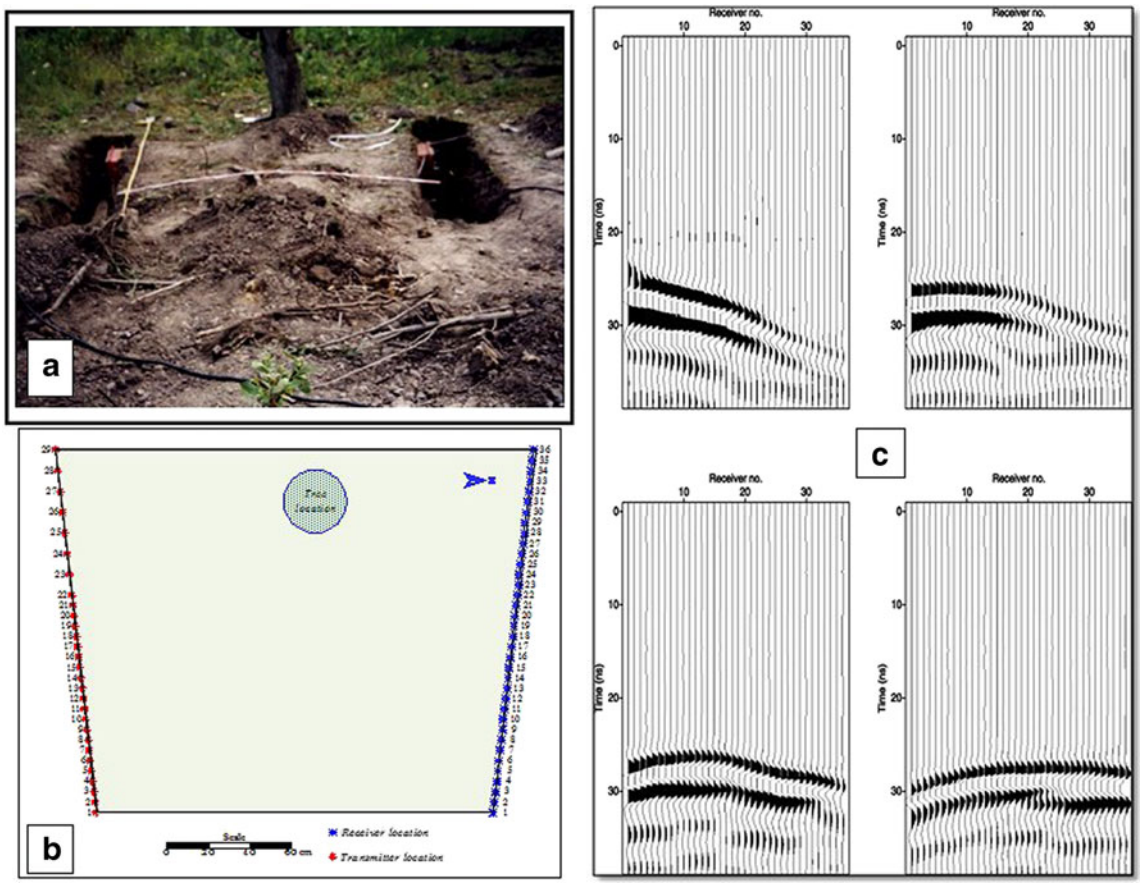

Fig. 4 Field GPR tomographic survey (phase I); **a** site photo of the poplar tree and the two trenches, **b** Tx, Rx and the target poplar tree layout base map, and **c** some processed radargrams at various Tx positions

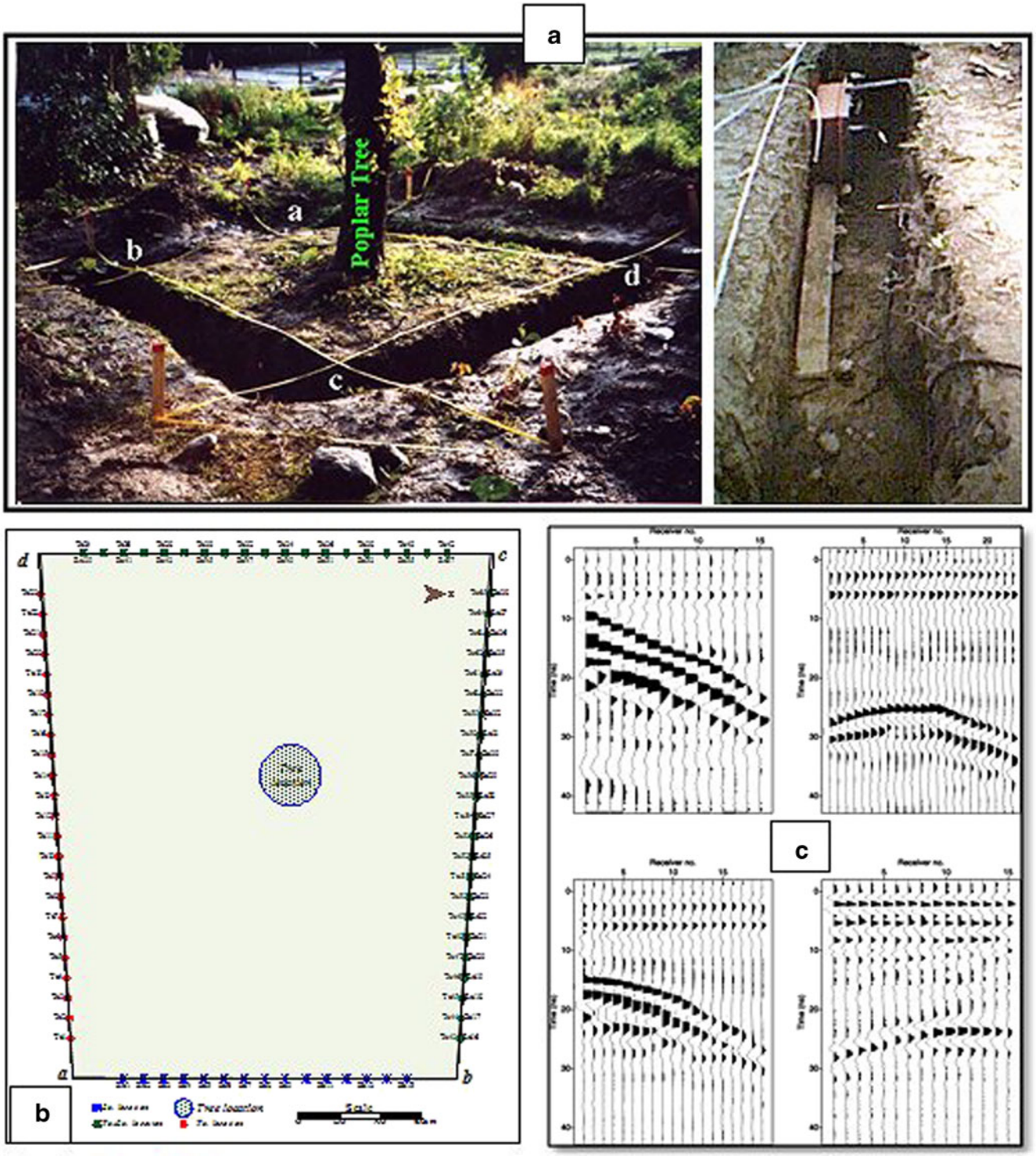

Fig. 5 Field GPR tomographic survey (phase II); **a** site photo of the poplar tree, the four trenches, and the antenna position during tomography data acquisition, **b** Tx, Rx and the target poplar tree layout base map, and **c** four samples of the processed radargrams at different Tx positions

study area. In other words, the antenna is moved along the *x*- or *y*-axis and the radargram is recorded along the *xy*-plane. The recorded GPR reflection data are performed using 16 trace stacking, 512 sampling interval, and time window of 40 ns. Figure 6 shows the raw radargrams of the performed four GPR reflection profiles. These data are filtered using 200–900 MHz band-pass filter and then a gain function (*T*-power of 2.5 order) is applied.

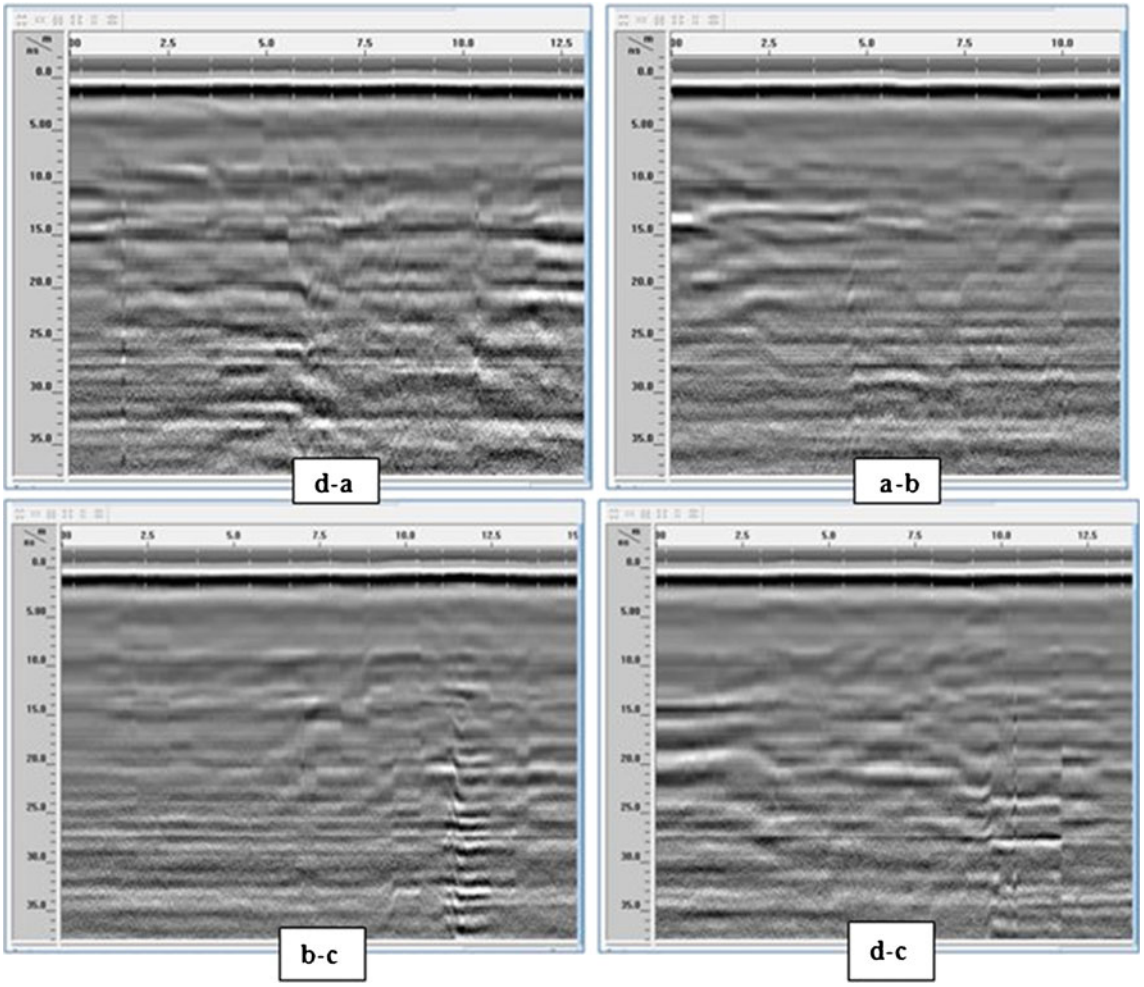

Fig. 6 Raw radargrams of the four GPR reflection profiles

Results

GPR tomography results

The radar tomographic data of the field surveys are inverted using the developed *SeismoRad* PC-code. The resulted GPR velocity tomogram of the first phase field experiment is shown as contour map in Fig. 7a. RMS error of 1.066 % is reached after 200 iterations between the measured and calculated times. The estimated GPR velocity values are ranging between 7.2 and 9.85 cm/ns (Fig. 7a). A relatively low radar velocity zone (7.2–7.9 cm/ns) could be outlined at the eastern side of the tomogram corresponding to the relative high water content within a zone that has been previously excavated for another experiment in the site. The effect of the root system of the poplar tree could not be clearly outlined in the resulted tomogram of the first phase due to insufficient rays passing through the tree location and that the poplar tree is not actually located at the middle of the survey zone where intensive rays are crossing.

The recorded GPR times of the second-phase field experiment are inverted and a final RMS error value of 5.7 % is obtained between the calculated and measured times after 200 iterations. The calculated GPR tomogram shows velocity ranging between 5.5 and 13.5 cm/ns (Fig. 7b). A high velocity value could be outlined at the extreme northeastern corner of the tomogram and could be due to root-free dry soil. Two low-velocity zones (8.14–8.76 cm/ns and 5.25–7.98 cm/ns) could also be delineated at the middle and at the southeastern corner of the tomogram, respectively. These anomalies are at the locations of the tree root zone and a previously excavated sector, respectively.

GPR reflection profile results

The recorded GPR reflection data are filtered using bandpass filter (200–900 MHz) and then a gain function is applied of the type *T*-power (2.5 order). Figures 8a and 9a show the resulted processed GPR reflection lines. At each

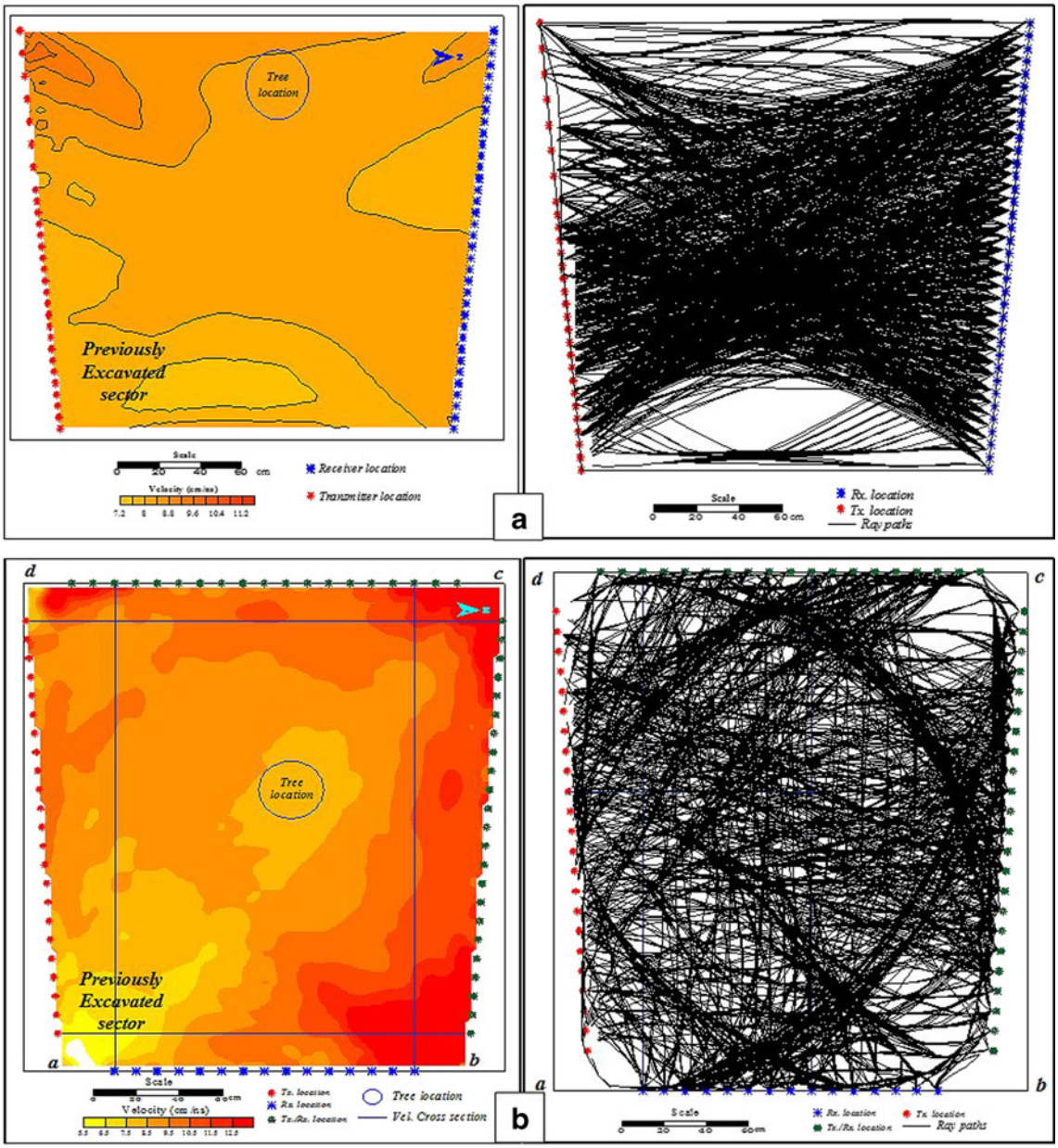

Fig. 7 **a**, **b** Calculated GPR velocity tomograms and the ray paths connecting (Tx) and (Rx) positions of the two field experiments phases I and II, respectively

radargram, three continuous, high-amplitude reflections could be traced and digitized to estimate their lateral extension (Figs. 8b and 9b). Four velocity cross sections are depicted from the four tomograms at the location of the four trenches (Figs. 8c and 9c).

These velocity sections are used to calculate the probing penetration distance of radar waves, which in fact is equivalent to the horizontal distance to reflections on the radargram as well as the horizontal distance to the top of the high-amplitude reflections (Figs. 8d and 9d). Since the surveyed area is consisting of wet to saturated mud without any sharp discontinuity, we do not expect to obtain sharp GPR reflections on the radargrams. However, on the four GPR reflection radargrams, relatively high-amplitude features are observed and outlined. These high-amplitude reflections can be attributed to the boundary between the saturated and wet zones, where different water contents affect the GPR velocity. Table 1 lists the positions of the delineated strong reflections, the calculated lateral distance to the top of each, and the suggested interpretation based on relative soil moisture content.

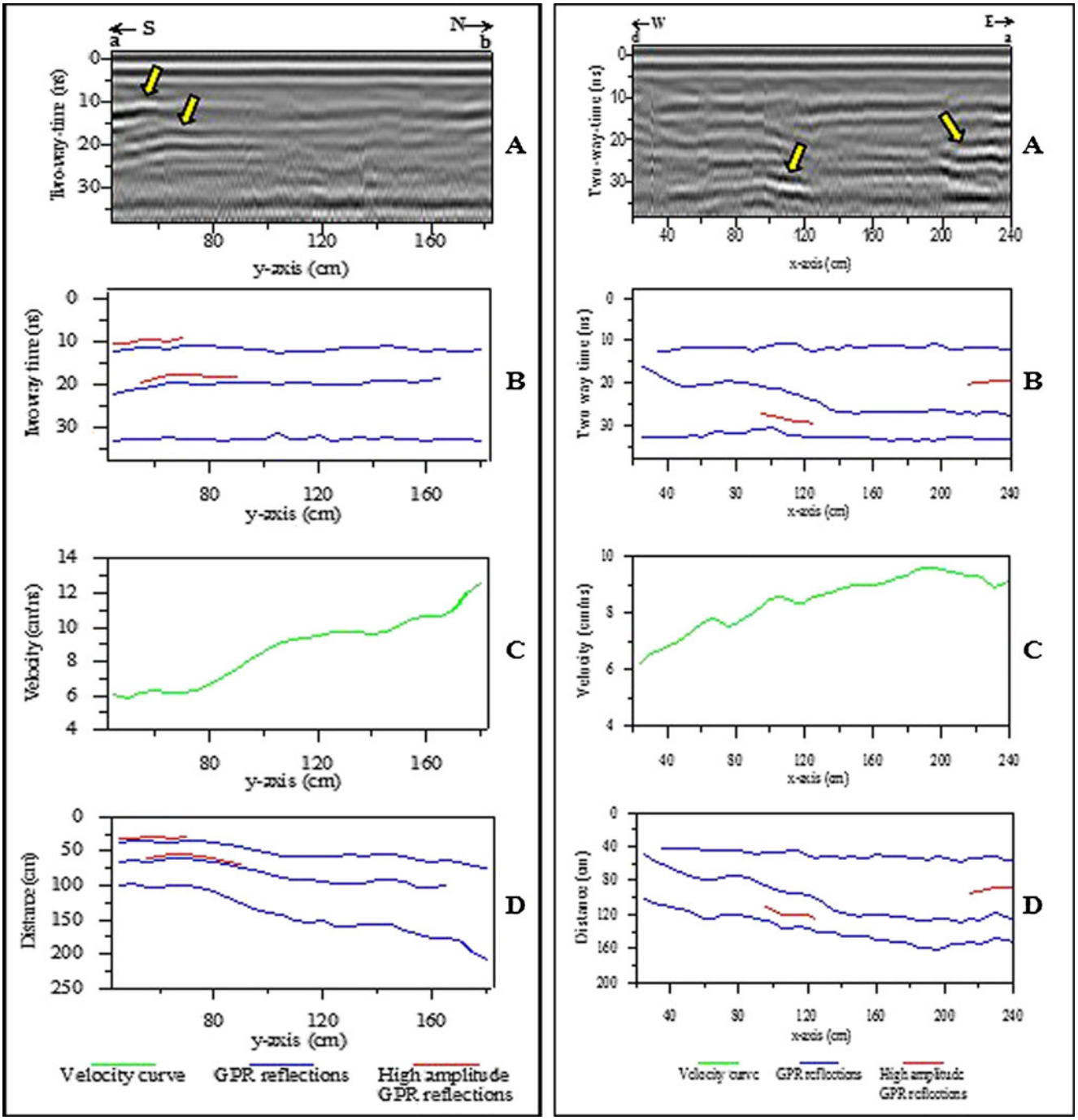

Fig. 8 GPR reflection lines (*a–b*) and (*d–a*). (*A*) Processed radargrams, (*B*) digitized reflectors, (*C*) Velocity section used for time–distance conversion, and (*D*) corresponding GPR-penetration distance cross-section

Discussion

The results of the GPR tomography analysis concluded that the Tx–Rx survey layout with respect to the target, here referred to the root system of the poplar tree, plays a vital role in delineating the target through identification of zones of different moisture content. Parallel Tx–Rx layout produces insufficient rays passing through the tree location and that the poplar tree is not actually located at the middle of the survey zone where intensive rays are crossing. Deployment of two orthogonal Tx and two orthogonal Rx increases the ray intensity in the investigated area and consequently enhance the target identification.

The processed tomographic radargrams of the first field experiment (phase I) exhibit relative low amplitude and frequency than that of the second phase due to the fact that, due to ineffective survey design in the first phase, no sharp

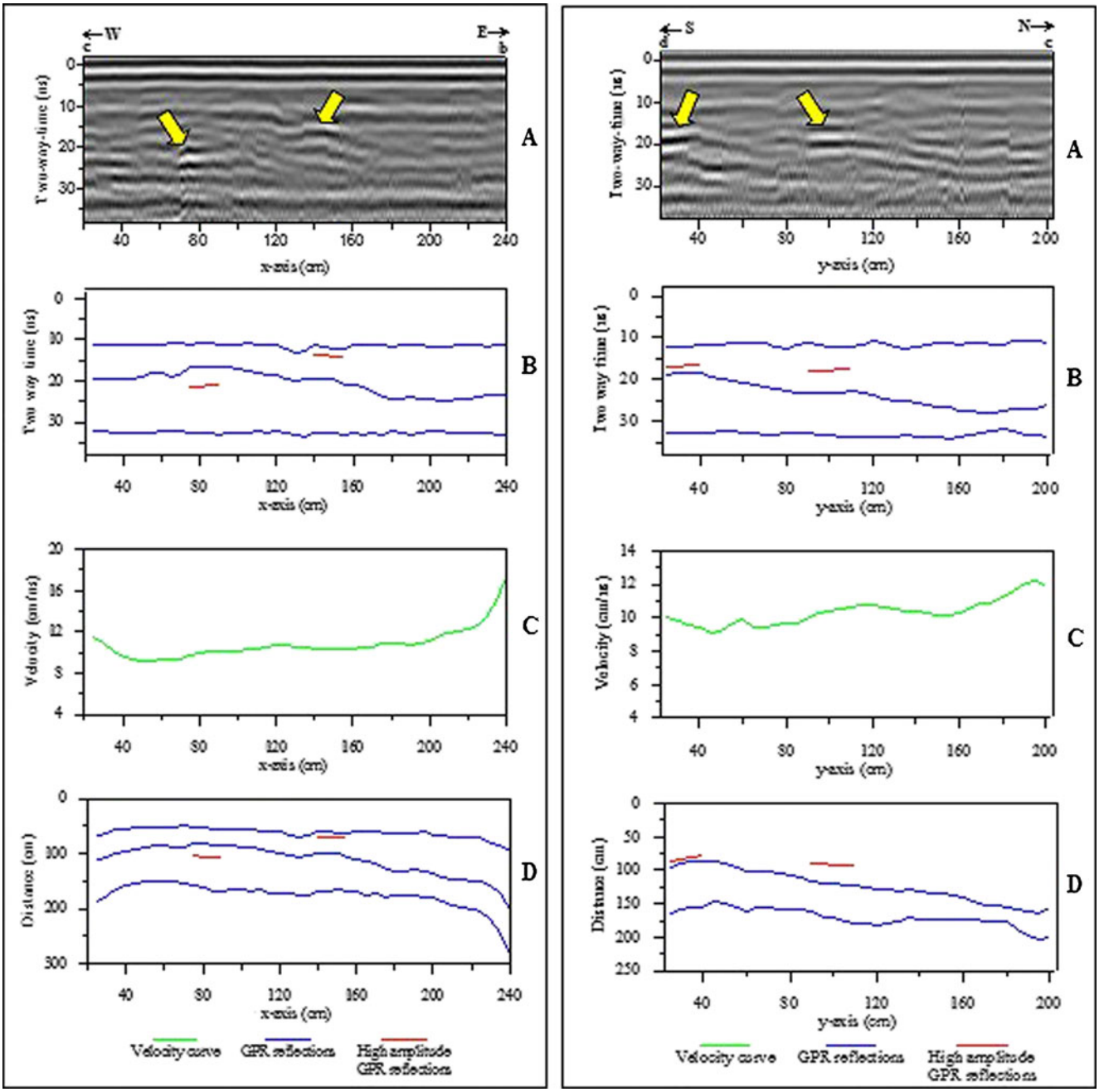

Fig. 9 GPR reflection lines (*c–b*) and (*d–c*). (*A*) Processed radargrams, (*B*) digitized reflectors, (*C*) Velocity section used for time-distance conversion, and (*D*) Corresponding GPR-penetration distance cross-section

discontinuity in radar velocity could be attained between areas of variable moisture content.

Figure 10 displays qualitative correlation between the GPR tomogram of the second phase of field experiment and the four radar reflection lines. The following facts are revealed from this comparison:

(a) The calculated tomogram displays radar velocity range of 5.5–13.5 cm/ns with relatively high velocity 11.5–13.5 cm/ns anomaly at the extreme northeastern corner due to root-free dry soil. Two low-velocity zones 8.14–8.76 cm/ns and 5.25–7.98 cm/ns at the middle and southeastern corner of the tomogram due to tree root zone and a previously excavated sector, respectively.

(b) The root system of the poplar tree and the previously excavated sectors that are observed on the calculated tomogram as low radar velocity zones are due to their relatively higher water content. Both are also observed on the radar reflection lines with high-amplitude reflections due to the relatively high radar velocity contrast between them and the surroundings.

Table 1 Summary of interpretation results of the GPR reflection profiles

GPR reflection profile ID	Position of delineated anomalous strong reflections (DASR)	Calculated distance to the top of DASR	Interpretation
d–a	x=95–125 cm twt=27.3–29.5 ns	111–125 cm	Tree root system
	x=215–240 cm twt=19.4–20.4 ns	89–95 cm	Previously excavated zone
a–b	y=45–70 cm twt=10.4–9.3 ns	28.8–31.5 cm	Previously excavated zone
	y=55–90 cm twt=19.3–18.1 ns	59.8–68.8 cm	Previously excavated zone
c–b	x=75–90 cm twt=21–21.5 ns	107–104.7 cm	Buried rock
	x=140–155 cm twt=13.5–13.9 ns	69.9–71.8 cm	Tree root system
d–c	y=25–40 cm twt=17–16.2 ns	86.2–77.2 cm	Low-GPR velocity zone
	y=90–110 cm	89.2–93.5 cm	Tree root system

Summary and conclusions

GPR tomography and reflection field experiments are performed, using a 500-MHz antenna, at the Botanic garden of Kiel University, Kiel, Germany, where relative soil moisture distribution around a poplar tree is investigated. The main aim of the experiments is to define the ability of both GPR survey modes to delineate relative soil moisture contents. The field GPR tomography experiment is carried out in two consecutive phases. In the first phase, two approximately parallel opposite trenches where 29 Tx are placed in one trench and 36 Rx are placed in the other one. As a result, ray

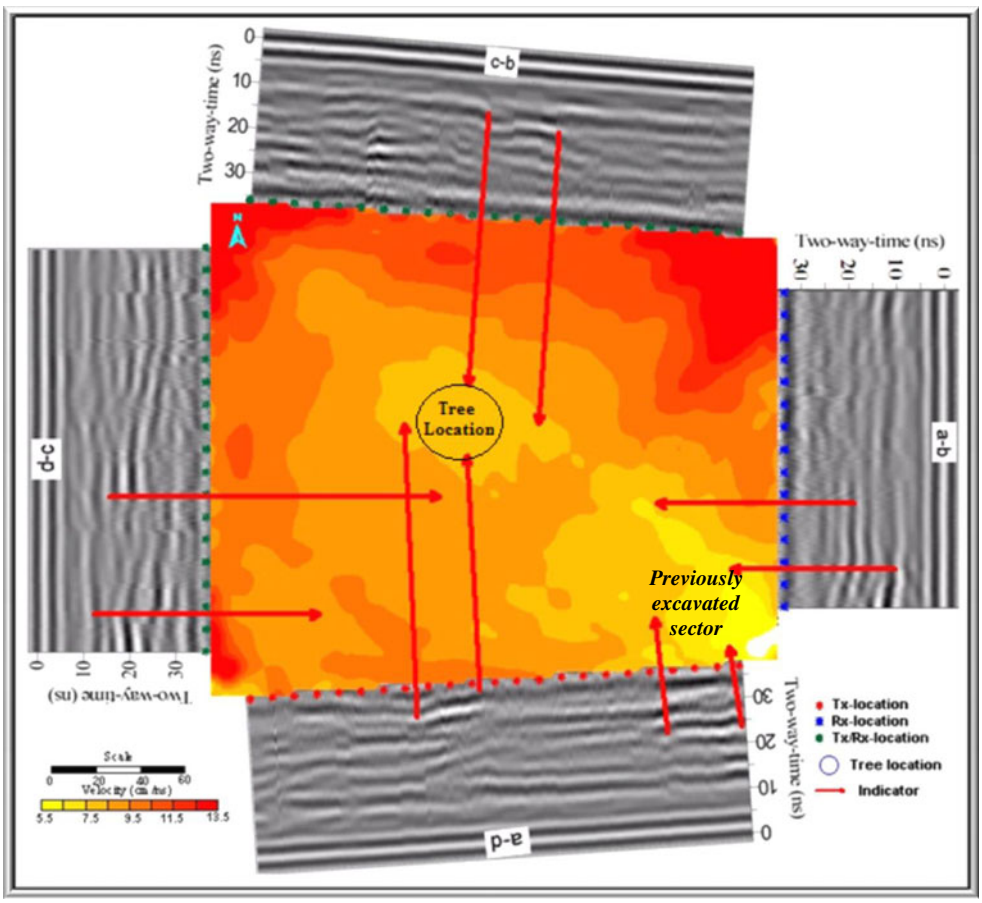

Fig. 10 Integrated GPR tomogram and reflection radargrams to image soil moisture characterized by low velocity and strong reflection

paths are recorded only in one direction and only 1,044 readings are recorded. In the second phase, the two existing trenches are added in length so that the poplar tree lies in the middle of the surveying site and two new trenches are excavated around the poplar tree, perpendicular to the old ones. Here 65 Tx and 57 Rx locations are set along the four sides of the trenches.

In this case, the ray paths come from all directions around the target and 2,213 GPR readings could be collected. The interpretation of the two phases proved that, using orthogonal shooting and receiving layout could enhance target identification due to intensive rays crossing the target.

The recorded radar tomographic data are inverted using software code *SeismoRad*, specially developed by the authors for inverting seismic and radar tomographic data based on the finite difference technique. The attained RMS errors after 200 iterations between the measured and calculated times range between 1.066 and 5.7 % in the two tomography experiments. The estimated GPR velocities are 7.2–9.85 cm/ns and 5.5–13.5 cm/ns in the first and second experimental phases, respectively. The effect of the root system of the poplar tree does not appear in the resulted tomogram of the first phase experiment due to inadequate rays passing through the tree location. Locations of the tree root system and previously excavated sector could be outlines in the tomogram of the second phase of field experiment by their distinguished low radar velocities (8.14–8.76 cm/ns and 5.25–7.98 cm/ns, respectively). Such decreases in GPR velocities are due to high moisture content. On the GPR reflection radargrams, relatively high-amplitude features are outlined and attributed to the boundary between zones of relative change in moisture content, where different water contents affect the GPR velocity. Comparable results with respect to zones of high moisture content are obtained between the GPR tomography and radar reflection results.

References

Annan AP (2005) Ground penetrating radar. In Near Surface Geophysics. In: Butler D (ed) Investigations in Geophysics No. 13: 357–434. SEG, Tulsa

Asprion, U (1998) Ground-penetrating radar (GPR) analysis in aquifer-sedimentology: Case studies, with an emphasis on glacial systems of SW Germany. Tuebinger Geowissenschaftliche Arbeiten, Reihe A, B-43

Baumgardt DZ, Der JC, Maxon M, Bell A (1995) Geological/geophysical modeling of seismic/GPR tomographic imaging for environmental applications. Symposium on Applied Geophysics Engineering Environmental Problems (SAGEEP) Proceedings, 519-528

Cai J, McMechan GA (1999) 2D ray-based tomography for velocity, layer shape, and attenuation from GPR data. Geophysics 64:1579–1593

Davis JL, Annan AP (1989) Ground-penetrating radar for high-resolution mapping of soil and rock stratigraphy. Geophys Prospect 37:531–551

Gerald CF, Wheatley PO (1989) Applied numerical analysis. Addison-Wesley, New York

Gerald H, Wollschaeger U, Yu Q, Schiwek Ph, Pan X, Roth K (2008) Continuous and simultaneous measurement of reflector depth and average soil-water content with multichannel ground-penetrating radar. Geophysics 73(4):J15–J23

Hanafy SM (2002) GPR/seismic tomography for delineating subsurface structures. PhD Dissertation, Cairo University, Egypt. P. 151

Hanafy S, al Hagrey SA (2006) Ground-penetrating radar tomography for soil-moisture heterogeneity. Geophysics 71, No. 1: K9-K18

Hinkle KM, Doolittle JA, Bockheim JG, Nelson FE, Paetzold R, Kimble JM, Travis R (2001) Detection of subsurface permafrost features with ground-penetrating radar, Barrow, Alaska. Permafr Periglac Process 12:179–190

Hole JA, Zelt BC (1995) 2D-Finite difference reflection traveltimes. Geophys J Int 121:427–434

Hubbard SS, Peterson JE Jr, Majer EL, Zawislanski PT, Williams KH, Roberts J, Wobber F (1997) Estimation of permeable pathways and water content using tomographic radar data. Lead Edge 16:1623–1628

Huisman JA, Hubbard SS, Redman JD, Annan AP (2003) Measuring soil water content with ground penetrating radar: a review. Vadose Zone J 2:476–491

Kowalsky MB, Finsterle S, Peterson J, Hubbard S, Rubin Y, Major E, Ward A, Gee G (2005) Estimation of field-scale soil hydraulic and dielectric parameters through joint inversion of GPR and hydrological data. Water Resour Res 41:W11425

Lambot S, Antoine M, van den Bosch I, Slob EC, Vanclooster M (2004) Electromagnetic inversion of GPR signals and subsequent hydrodynamic inversion to estimate effective Vadose Zone hydraulic properties. Vadose Zone J 3:1072–1081

Lo T–w, Inderwiesen Ph (1994) Fundamentals of seismic tomography. No. 6. In Geophysical Monograph Series, Fitterman D. (Ed.), SEG, Tulsa, USA

Menke W (1989) Geophysical data analysis: discrete inverse theory. Academic, San Diego, CA

Moorman BJ, Robinson SD, Burgess MM (2003) Imaging periglacial conditions with ground-penetrating radar. Permafr Periglac Process 14:319–329

Neal A (2004) Ground-penetrating radar in sedimentology: principles, problems and progress. Earth Sci Rev 66:261–330

Peterson JE Jr (2001) Pre-inversion correlations and analysis of radar tomographic data. J Environ Eng Geophys 6:1–18

Rea J, Knight R (1998) Geostatistical analysis of ground-penetrating radar: a means of describing spatial variation in the subsurface. Water Resour Res 34:329–339

Roth K, Wollschaeger U, Chang ZH, Zhang JB (2004) Exploring soil layers and water tables with ground-penetrating radar. Pedosphere 14(3):273–282

Schmalholz J, Stoffregen H, Kemna A, Yaramanci U (2004) Imaging of water content distributions inside a lysimeter using GPR tomography. Vadose Zone J 3:1106–1115

Valle S, Zanzi L (1996) Radar tomography for cavities detection. Symposium on Applied Geophysics Engineering Environmental Problems (SAGEEP) Proceedings: 555-563

van Overmeeren RA, Sariowan SV, Gehrels JC (1997) Ground penetrating radar for determining volumetric soil water content: results of comparative measurements at two test sites. J Hydrol 197:316–338

Vasco DW, Peterson JE Jr, Lee KH (1997) Ground-penetrating radar velocity tomography in heterogeneous and anisotropic media. Geophysics 62:1758–1773

Vidale J (1990) Finite-difference calculation of traveltimes in three dimensions. Geophysics 55:521–526

Wollschlaeger U, Roth K (2005) Estimation of temporal changes of volumetric soil water content from ground-penetrating radar reflections. Subsurf Sens Technol Appl 6:207–218

Wollschlaeger RK, Cheng ZH, Zhang JB (2004) Exploring soil layers and water tables with ground-penetrating radar. Pedosphere 13:273–282